Check for updates

Proceedings of the ASME 2021 40th International Conference on Ocean, Offshore and Arctic Engineering
OMAE2021
June 21-30, 2021, Virtual, Online

OMAE2021-62774

Downloaded from http://asmedigitalcollection.asme.org/OMAE/proceedings-pdf/OMAE2021/85192/V009T09A027/6780842/v009t09a027-omae2021-62774.pdf by NTNU Universitets Biblioteket user on 01 April 2022

VALIDATION OF A NUMERICAL MODEL FOR THE INVESTIGATION OF TENSION LEG PLATFORMS WITH MARINE ENERGY APPLICATION USING REEF3D

Christian Windt*
Leichtweiß-Institute for Hydraulic Engineering and Water Resources
Technische Universität Braunschweig
Braunschweig, Germany

Nils Goseberg
Leichtweiß-Institute for Hydraulic Engineering and Water Resources
Technische Universität Braunschweig
Braunschweig, Germany

Tobias Martin
Department of Civil and Environmental Engineering
Norwegian University of Science and Technology
Trondheim, Norway

Hans Bihs
Department of Civil and Environmental Engineering
Norwegian University of Science and Technology
Trondheim, Norway

ABSTRACT

Exploiting the offshore wind resources using floating offshore wind systems at sites with deep water depths requires advanced knowledge of the system behaviour, including the hydro-, areo-, and mooring dynamics. To that end, high–fidelity numerical modelling tools, based on Computational Fluid Dynamics, can support the research and development of floating offshore wind systems by providing high–resolution data sets.

This paper presents the first steps towards the numerical modelling of tension leg platforms for floating offshore wind applications using the open–source Computational Fluid Dynamics toolbox REEF3D. The numerical model of a taut–moored structure is validated against experimental reference data. Results from wave–only test cases highlight the simplicity and effectiveness of the wave generation method, implemented in REEF3D. For the considered wave-structure interaction cases, deviations between the experimental and numerical data can be observed for the surge and pitch displacements, while the heave displacement and the mooring forces are capture with sufficient accuracy. Overall, the numerical results indicate high potential of REEF3D to be used for the modelling of floating offshore wind systems

1 Introduction

Offshore renewable energies and, in particular, offshore wind energy plays a significant role in tackling human–induced climate change and global warming. To increase the production efficiency and further exploit the capacity of offshore wind, the industry is progressing towards the commercialisation of floating offshore wind turbines (FOWT). Being based in locations with deep water depths ($> 50\,\mathrm{m}$), the mooring of FOWTs becomes an eminent aspect during the device design. To that end, different mooring systems, such as catenary or taut mooring, have been considered to moor floating offshore wind applications [1].

Floating structures with taut mooring systems, i.e. tension leg platform (TLP) type systems, are beneficial in terms of, e.g., the relatively small footprint of the overall system, compared to catenary mooring systems, and their relatively small pitch motion [2]. As an example, Figure 1 shows an idealised schematic of a TLP–type floating structure for offshore wind applications.

*Address all correspondence to this author.

Copyright © 2021 by ASME

An example of a TLP-type floating structure for offshore wind applications, currently under development, can be found, e.g., in [3].

During the design of FOWTs and the mooring system, high-fidelity numerical models, based on Computational Fluid Dynamics (CFD), including accurate descriptions of both the wave–structure interaction (WSI) and the mooring dynamics, render a valuable complement to experimental model testing. Avoiding, e.g. scale limitations and allowing the measurement of relevant quantities throughout the entire computational domain without interfering with model setup, such high-fidelity numerical models alleviate some of the well-known problems of physical wave tank testing, such as scale and model effects. Some examples of relevant study are reviewed in the following.

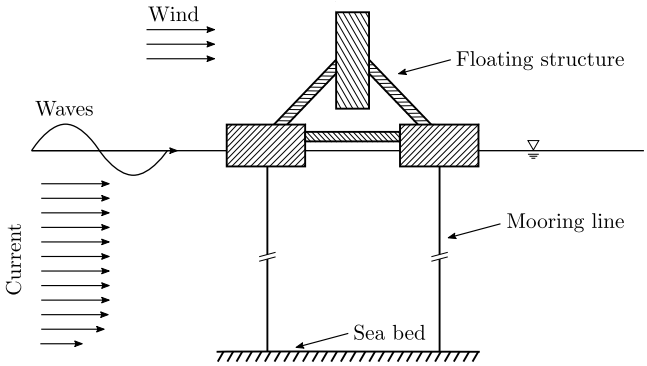

FIGURE 1: Schematic of a floating, TLP–type, structure for offshore wind applications, exposed to wind, wave, and current loads. The wind turbine is mounted on on top of the floating structure exerting additional loads.

1.1 Related studies

Ren et al. [4] simulate a TLP–type FOWT system for a 5 MW wind turbine. For the implementation of the hydro-aerodynamic model, the authors choose the ANSYS FLUENT software, with which they model wind–wave cases. The sliding mesh method is used to accommodate the motion of the FOWT; however, the authors only considered the surge degree of freedom (DoF), while oppressing the motion in any other DoF. The loads on the mooring system, i.e. tension legs, are considered via a linear stiffness in the surge DoF. Comparing the numerical results to experimental reference data, the authors find "good agreement" and attribute the observed differences to the constrained device motion, i.e. single DoF simulation.

Also studying a TLP–type FOWT system, Nematbakhsh et al. [2] validate a coupled fluid–structure interaction model, based on CFD and a two–body rigid body model. Results are compared against numerical reference data, based on potential flow theory. In the structural model, the tendons are presented as simple spring–damper systems and forces from the structural model are fed to the CFD solver in a one–way fashion. The presented study includes free decay tests, as well as WSI simulation in regular waves. Overall, good agreement is identified between the presented numerical model and the reference. Notable differences are, however, found for the surge motion of the systems, which the authors explain by nonlinear effects of the wave loads. Furthermore, it is found that tendon forces are governed by the pitch response of the system.

Quallen et al. [5] develop an aero-hydrodynamic model, based on CFDShip-Iowa V4.5, for the spar-buoy FOWT Hywind model, including a quasi–static mooring model for the crowfoot mooring system. While the model neglects bending stiffness and dynamic effects, the weight of the mooring line, elastic stretching, and seabed friction are accounted for. In a follow–up study, [6], the authors use the numerical model to study a variable–speed generator–torque controller. To that end, the numerical model is extended with a model for the inertial drivetrain model and variable–speed controller. The study includes cases of a fixed and dynamic structure, where, for the latter, a comparison to NREL's FAST modelling tool shows, amongst others, a reduction of the mean surge and pitch motion, which is attributed to differences in the mooring forces.

Liu et al. [7] study a semi-submersible floating offshore wind system with an NREL 5 MW baseline wind turbine. The paper presents a fully coupled aero-hydro model, based on the CFD toolbox OpenFOAM, including a quasi-static mooring line analysis model for the catenary mooring system. With the model, the authors aim to investigate the wind turbine aerodynamics, the floating platform hydrodynamics and mooring dynamics, as well as the aero-hydrodynamic coupling. Within OpenFOAM, sliding meshes are used to accommodate the motions of the rotor, as well as the floating structure in the three DoFs surge, heave, and pitch. Analysing the influence of the wind turbine on the floating platform, the authors find that the aerodynamic thrust induced additional surge and pitch motion and, thereby, leads to additional mooring loads. Ultimately, the authors concluded that the obtained results from the high–fidelity model are in line with lower–fidelity models, allowing, in addition, the detailed analysis of the flow field around a FOWT. A similar study, using STAR–CCM+ as modelling framework, can be found in [8].

More recently, Burmester et al. [9] perform a study on the uncertainty, related to high–fidelity modelling of FOWT using reFresco. Amongst others, the authors include a test case of a surge free decay test for the DeepCwind semi-submersible (see also [10] for detailed information on the surge decay simulation). Only the floating structure is directly modelled, while, e.g., the nacelle and turbine are only included via its physical properties (i.e. mass, inertia, etc.). The (catenary) mooring system is represented via stiffness values for all six DoFs. For the surge decay test, the authors compare three different methods to estimate the discretisation uncertainty and compare results to experimen-

Downloaded from http://asmedigitalcollection.asme.org/OMAE/proceedings-pdf/OMAE2021/85192/V009T09A027/6780842/v009t09a027-omae2021-62774.pdf by NTNU Universitets Biblioteket user on 01 April 2022

Copyright © 2021 by ASME

tal data. During the validation, discrepancies of up to 37.3% are found, which are, amongst others, attributed to errors in the mooring model.

The reviewed literature indicates that various modelling frameworks are used for the aero-hydrodynamic and mooring model. Furthermore, a focus on the modelling of FOWTs in conjunction with a catenary mooring system can be identified. In contrast, this study presents the first step towards a high-fidelity numerical model of a floating, TLP–type, structure for offshore wind applications using the open–source CFD modelling toolbox REEF3D [11]. REEF3D solves the Reynolds-averaged Navier-Stokes equations[1], discretised using the finite difference method in conjunction with high-order spatial and temporal discretisation schemes. The free surface is captured with the level set method and free-surface waves are generated and absorbed by means of the relaxation zone method.

In particular, this paper presents the validation of a tautly moored floating structure, exposed to focused wave groups. The validated model will form the basis for the analysis of a floating, TLP–type, structure for offshore wind applications as pertinent future work. The reference data set, employed in this study, is taken from the CCP-WSI Blind Test Studies 2 and 3, documented in [12] and [13], respectively. The employed reference model presents a significant simplification, compared to a TLP–type FOWT. However, it must be noted that well documented benchmark cases for TLP–type FOWT systems are not easily accessible. The data set, used within this study, has been used in multiple validation studies by various authors [12, 13], rendering a trustworthy reference for model validation.

The remainder of this paper is organised as follows. Section 2 introduces the case study, used for the presented validation of the numerical model. Following on, Section 3 details the numerical wave tank (NWT), including the numerical methods within REEF3D, as well as the numerical wave generation and absorption method, and the problem discretisation. With the numerical setup detailed in Section 3, simulations are performed and the results are presented and discussed in Section 4. Finally, conclusions are drawn in Section 5.

2 Case study

Due to the lack of a sufficient data set for the validation of a floating TLP-type structure, this study resorts to the case study of a floating, taut-moored buoy, exposed to focused waves. The case study has initially been designed for the CCP-WSI Blind Test Studies 2 and 3, documented in [12] and [13], respectively.

The experimental tests, of which the data is used as the reference in this study, were conducted in the ocean basin of the COAST Laboratory at the University of Plymouth, UK. A schematic of the wave basin, including all relevant dimensions, is shown in Figure 2. Both wave-only and WSI experiments were conducted. The water depth is set to 3m throughout the tests.

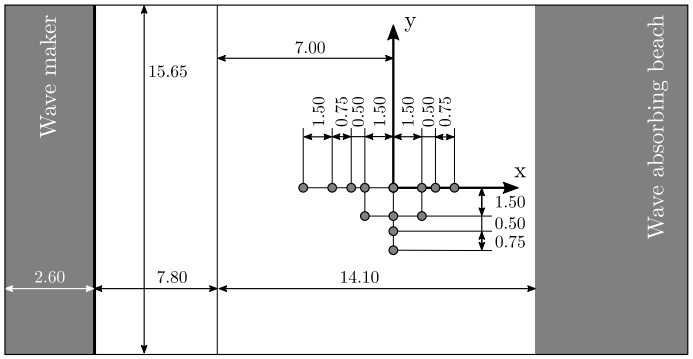

FIGURE 2: Top view schematic (not to scale) of the physical wave tank (dimensions in [m]). For the WSI experiments, the floating structure is placed at the location of the origin of the coordinate system. The grey markers identify the location of the wave probes.

During the experimental tests, two different floating, taut-moored structures were considered, both with axisymmetric, cylindrical, geometries. While one of the structures features a moon-pool and sharp–cornered edges, the other structure features a hemispherical bottom shape. For the sake of brevity, only the latter structure will be considered herein. The relevant physical dimensions of the floating structure are shown in Figure 3. Other relevant physical properties are listed in Table 1. The taut–mooring of the structures was implemented with a linear spring, with a stiffness of $67\,\mathrm{N\,m^{-1}}$, connecting the device with the tank floor. During the experiments, the structure was initially placed at the location of the origin of the coordinate system in Figure 2.

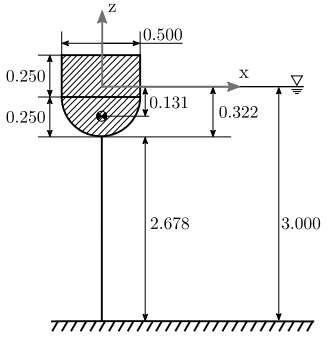

FIGURE 3: Schematic of the considered floating structure (dimensions in [m]).

[1]It should be noted that laminar flow conditions are assumed throughout this study

Copyright © 2021 by ASME

Downloaded from http://asmedigitalcollection.asme.org/OMAE/proceedings-pdf/OMAE2021/85192/V009T09A027/6780842/v009t09a027-omae2021-62774.pdf by NTNU Universitets Biblioteket user on 01 April 2022

TABLE 1: Properties of the considered floating structure

Mass	[kg]	43.674
Ixx	[kg m^2]	1.620
Iyy	[kg m^2]	1.620
Izz	[kg m^2]	1.143
Mooring Pretension	[N]	32.070

To excite the floating structure, three focused wave groups of varying wave steepness were considered. The characteristics of the focused wave groups is listed in Table 2. Free surface time histories of the focused waves groups, measured at the spatial focal point (origin of the coordinate system in Figure 2), are shown in Figure 4. Note that the wave traces are artificially aligned to match the peak at the focal point in time.

TABLE 2: Characteristics of the three considered focused waves

ID	A_n [m]	f_p [Hz]	H_s [m]	λ_p [m]	kA [-]
#1	0.25	0.3578	0.274	11.35	0.129
#2	0.25	0.4	0.274	9.41	0.161
#3	0.25	0.4382	0.274	7.99	0.193

A_n: Peak wave amplitude; f_p: Peak wave frequency;

H_s: significant wave height; λ: wave length; k: wave number

3 Numerical wave tank

The hydrodynamics within the NWT are captured by solving the incompressible Navier–Stokes equations, describing the conservation of mass and momentum:

$$\nabla \cdot \mathbf{U} = 0 \tag{1}$$

$$\frac{\partial \mathbf{U}}{\partial t} + \nabla \cdot \mathbf{U}\mathbf{U} = -\frac{1}{\rho}\nabla p + \nabla \cdot (\nu \nabla \mathbf{U}) + \mathbf{f}_b\,, \tag{2}$$

respectively. Here, t denotes time, $\mathbf{U}$ is the fluid velocity, p the fluid pressure, ρ the fluid density, $\mathbf{f}_b$ the external forces such as gravity, and ν the kinematic viscosity [14]. Note that, based on [15], laminar flow conditions are assumed throughout this study.

3.1 Fluid dynamics solver

In this study, the open–source CFD toolbox REEF3D [11] is used for the solution of Equations (1) and (2). Within REEF3D, a rectilinear staggered grid is generated, and the velocities and source terms are defined on the cell faces. The pressure is stored in the cell centres so that a tight coupling between pressure and velocity is ensured. Finite differences are used to discretise the terms in space and time. The convection terms are discretised with fifth-order accurate weighted essentially non-oscillatory (WENO) schemes [16,17]. The Laplacian terms, such as the diffusion term, are handled by second-order accurate central differences. This term is further discretised with an implicit Euler method in time to remove it from the CFL condition. An n-halo domain decomposition strategy with three layers of ghost cells is implemented in REEF3D. The inter-processor communication is organised with the message passing interface (MPI) for maximum efficiency.

The incremental pressure-correction algorithm in [18] is implemented to solve the system of equations explicitly. The third-order accurate TVD Runge-Kutta scheme [19] is employed for the propagation in time. Here, a velocity field is predicted first using the pressure gradients of the previous Runge-Kutta substep $j-1$:

$$\frac{\mathbf{U}^{(*)} - \alpha_k \mathbf{U}^{(n)}}{\alpha_j \Delta t} = \frac{\beta_j}{\alpha_j}\mathbf{U}^{(j-1)} - \frac{\nabla p^{(j-1)}}{\rho} - \mathbf{U}^{(j-1)} \cdot \nabla \mathbf{U}^{(j-1)} + \mathbf{f}_b^{(*)}, \tag{3}$$

with $\alpha_j = 1.0, 1/4, 2/3$, $\beta_j = 0.0, 3/4, 1/3$ and $j = 1,2,3$. The diffusion term is included in the external force term. Next, a new pressure increment p_{inc} is obtained from the solution of the Poisson equation with the pressure correction term p_{corr} calculated from the Poisson equation

$$\nabla \cdot \left(\frac{1}{\rho}\nabla p_{\text{inc}}\right) = \frac{1}{\alpha_j \Delta t}\nabla \cdot \mathbf{U}^{(*)}. \tag{4}$$

The problem is solved using the parallelized BiCGStab algorithm with geometric multigrid preconditioning of the HYPRE library [20]. The updated pressure and velocity fields are finally calculated using

$$p^{(j)} = p^{(j-1)} + p_{\text{inc}} - \rho \nu \, \nabla \cdot U^{(*)}, \tag{5}$$

$$\mathbf{U}^{(j)} = \mathbf{U}^{(*)} - \frac{\alpha_j \Delta t}{\rho}\nabla p^{(j)}, \tag{6}$$

3.2 Free surface propagation

The free surface is implicitly defined using the zero level set of the signed distance function Φ. The propagation of the

Downloaded from http://asmedigitalcollection.asme.org/OMAE/proceedings-pdf/OMAE2021/85192/V009T09A027/6780842/v009t09a027-omae2021-62774.pdf by NTNU Universitets Biblioteket user on 01 April 2022

Copyright © 2021 by ASME

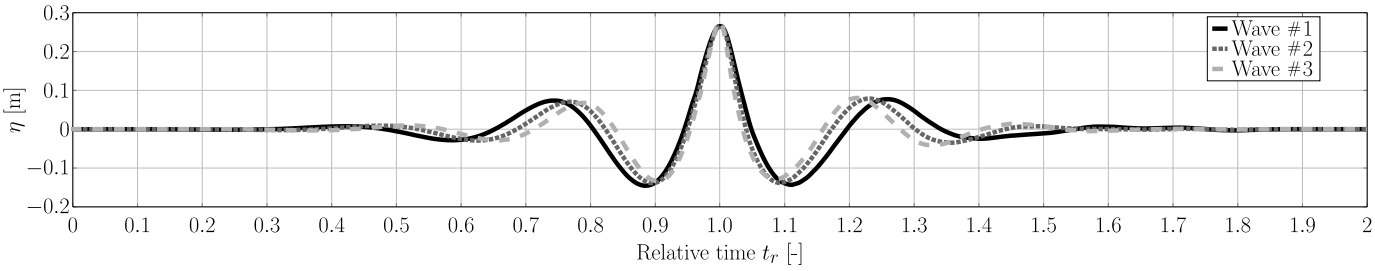

FIGURE 4: Experimentally measured surface elevation, η, of waves #1 – #3, at the focal location.

interface in space and time is calculated by solving the linear advection equation [21]

$$\frac{\partial \Phi}{\partial t} + \mathbf{U} \cdot \nabla \Phi = 0, \tag{7}$$

Equation (7) is discretised using the a WENO scheme for the spatial and the TVD Runge-Kutta scheme for the temporal term. Even though high order schemes are applied, the level set function has to be reinitialised after each time step to ensure its signed distance properties. For this purpose, a PDE-based reinitialisation algorithm [22] is utilised.

3.2.1 Numerical wave generation and absorption

For the generation and absorption, the relaxation zone method, implemented in REEF3D, is employed in this study. Two relaxation zone are defined towards the up– and down–wave boundaries of the domain with a length of $1\lambda_{p,\mathrm{W1}}$, i.e. 11.35 m. The lengths of the relaxation zones follow previous NWT setups with REEF3D. The interested reader is referred to [11] for more information on the implementation of the relaxation zone method. A schematic of the computational domain is depicted in Figure 5.

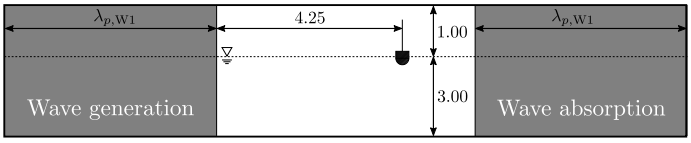

FIGURE 5: Schematic (not to scale) of the NWT, highlighting the wave generation and absorption relaxation zones.The floating structure is place 4.25 m away from the end of the wave generation relaxation zone, representing the distance between the first wave probe and the floating structure in the experimental setup (see Figure 2).

In contrast to approaches which require the calibration of the numerical wave generation method [23] or the manual decomposition of the input wave trace into its frequency components [24], REEF3D offers the possibility to generate the desired input focused waves groups at a specific focal point in space and time based on a set of user inputs. In particular, the user defines the number of frequency components, the focal time and point, the focused wave height, and the peak wave period. This renders the generation of focused waves groups simple and, as shown in Section 4, effective.

3.3 Floating body solver

Similarly to the free surface representation, a level set function Φ_{fb} is defined to implicitly represent the floating body in the domain, avoiding the use of dynamic mesh motion methods. A continuous direct forcing method [25] is employed to incorporate the kinematic and dynamic boundary conditions at the fluid-body interface into the momentum equations. As shown in [26], a forcing term

$$\mathbf{f}_{fb} = H(\Phi_{fb}^{(*)}) \cdot \left(\frac{\mathbf{P}(\mathbf{U}^{(*)}) - \mathbf{U}^{(*)}}{\alpha_j \Delta t} \right), \tag{8}$$

can be defined for this purpose. Here, $H(\Phi_{fb})$ is the smoothed Heaviside step function

$$H(\Phi) = \begin{cases} 0 & \text{if } \phi < -\varepsilon \\ \frac{1}{2}\left(1 + \frac{\Phi}{\varepsilon} + \frac{1}{\pi} sin(\frac{\pi \Phi}{\varepsilon})\right) & \text{if } |\Phi| \leq \varepsilon \\ 1 & \text{if } \Phi > \varepsilon, \end{cases} \tag{9}$$

with $\varepsilon = 2.1\Delta x$ and Δx a characteristic cell length. Further, $\mathbf{P}(\mathbf{U})$ is the velocity field projected onto a rigid body velocity field:

$$\mathbf{P}(\mathbf{U}^{(*)}) = \dot{\mathbf{X}}_{\mathbf{fb}} + \omega_{\mathbf{fb}} \times \mathbf{x}. \tag{10}$$

The translational rigid body velocities $\dot{\mathbf{X}}_{\mathbf{fb}}$ and $\omega_{\mathbf{fb}}$ are calculated from the conservation laws of translational and rotational impulse for rigid bodies. The equations are converted into a first-order system [27] which is solved with a 3rd-order Runge-Kutta

Downloaded from http://asmedigitalcollection.asme.org/OMAE/proceedings-pdf/OMAE2021/85192/V009T09A027/6780842/v009t09a027-omae2021-62774.pdf by NTNU Universitets Biblioteket user on 01 April 2022

Copyright © 2021 by ASME

scheme. The fluid forces and momenta acting on the floating structure are calculated from the discrete integration of the fluid properties at the interface between solid and fluid. Other external forces, such as the mooring tension forces, are added explicitly to the rigid body dynamics equations.

Once Equation (8) is determined, the term is added to the predicted velocity field before solving the Poisson equation.

3.4 Discretisation

To determine the required spatial discretisation, convergence studies for a wave–only, as well as a heave and surge free–decay test are performed, using three different cell sizes. Cell stretching is employed towards the boundaries of the domain, so that the smallest cell size are located in the vicinity of the floating structure and the free surface interface. Following the convergence analysis described in [28], a figure of merit, the relative discretisation uncertainty, $\mathscr{U}$, can be evaluated with the results for three different discretisation levels.

3.4.1 Waves–only For the wave–only test cases, the peak wave amplitude is used as input to the convergence study. By way of example, Figure 6 shows the free surface elevation time histories of wave #2, measured at the intended location of the structure, for three different cell sizes 0.0563 m, 0.0375 m, 0.0250 m, i.e. 4, 7, and 10 cells per peak wave amplitude (CPA). Table 3 lists the results of the peak wave amplitude and the relative discretisation uncertainty $\mathscr{U}$ for waves #1 – #3. Relatively small values of $\mathscr{U}$ are found, with a maximum discretisation uncertainty of 3.0% for wave #3.

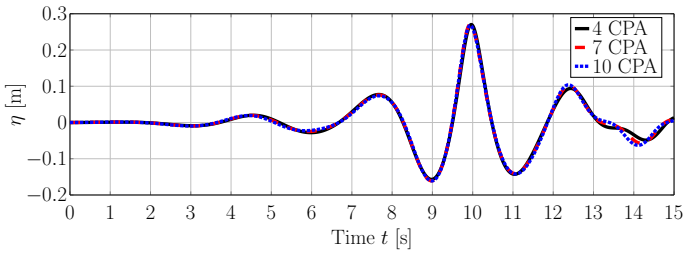

FIGURE 6: Time traces of the free surface elevation of wave #2, measured at the intended location of the structure, for three different cell sizes 4, 7, and 10 CPA.

3.4.2 Heave free–decay test For the heave free–decay test case, the mean peak–to–peak period, T_{p2p}, of the system is used as input to the convergence study. The floating structure, with the mooring system in place, is initially displaced by 0.1 m away from its vertical equilibrium position. A reduced numerical domain is used for the free–decay test, to accelerate the numerical simulations. Relaxation absorption zones of 0.4 m length are implemented towards the boundaries of the domain to prevent spurious reflections from the tank walls.

TABLE 3: Results of the wave–only convergence study

	A_n [m]			$\mathscr{U}$ [%]
	4 CPA	7 CPA	10 CPA	
#1	0.266	0.267	0.265	1.3
#2	0.270	0.271	0.268	1.8
#3	0.272	0.273	0.268	3.0

The time history of the relative heave position (relative to the location of the centre of gravity in equilibrium) is shown in Figure 7 for three different cell sizes 7, 10, and 15 CPA. It can readily be seen that the cell size has a larger influence on the results for the free–decay test, compared to the wave–only test case. This is also the justification for an additional decrease in cell size, i.e. 15 CPA, considered here. Table 4 lists the results of the mean T_{p2p} and the relative discretisation uncertainty $\mathscr{U}$. A discretisation uncertainty of 3.3% is found for the heave free–decay test.

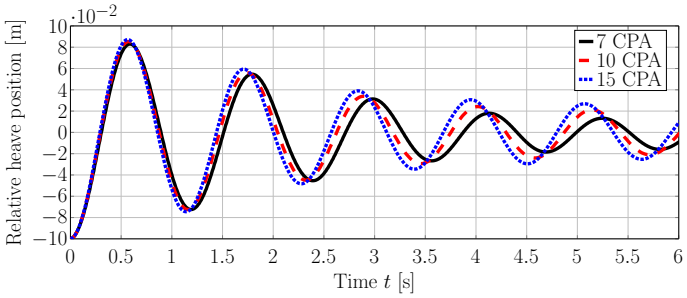

FIGURE 7: Time traces of the relative heave position of the floating structure for three different cell sizes 7, 10, and 15 CPA.

TABLE 4: Results of the heave free–decay convergence study

	T_{p2p} [s]			$\mathscr{U}$ [%]
	7 CPA	10 CPA	15 CPA	
Heave free-decay	1.18	1.14	1.13	3.3

Downloaded from http://asmedigitalcollection.asme.org/OMAE/proceedings-pdf/OMAE2021/85192/V009T09A027/6780842/v009t09a027-omae2021-62774.pdf by NTNU Universitets Biblioteket user on 01 April 2022

Copyright © 2021 by ASME

3.4.3 Surge free–decay test For the sake of brevity, only a qualitative comparison between different grid sizes is performed for the surge free–decay test case. Here, the floating structure is initially displaced by 0.1 m away from its horizontal equilibrium position.

The time trace of the relative surge position (relative to the location of the centre of gravity in equilibrium) is shown in Figure 8 for three different cell sizes 7, 10, and 15 CPA. As for the heave free decay test, it can readily be seen that the cell size has a relatively large influence on the results, resulting in varying amplitudes and periods of the oscillation. This may be caused by the close correlation between the accuracy of capturing boundary layer effects and the grid resolution due to the application of the immersed boundary method.

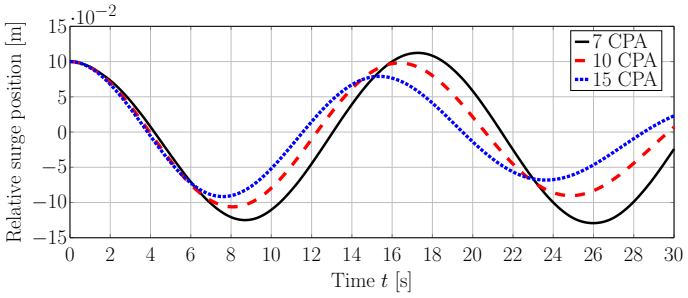

FIGURE 8: Time traces of the relative heave position of the floating structure for three different cell sizes 7, 10, and 15 CPA.

Ultimately, a cells size of 10 CPA is used throughout the remainder of this study. Employing cell stretching towards the far field boundaries of the domain and using a domain width to 4 m, an overall cell count of $\sim$ 6.8M cells can be achieved. A screenshot of the numerical domain, including all relevant dimensions, is shown in Figure 9.

4 Results and discussion

In this section, the results from the numerical simulation for the wave–only and WSI tests are shown and discussed. For a qualitative comparison with the experimental reference data, time traces of the relevant quantities (free surface elevation, mooring forces, heave, surge, and pitch displacement) are shown. For the quantitative comparison, the normalised root–mean–square error (nRMSE) is considered, following:

$$\mathrm{nRMSE} = \sqrt{\frac{\sum_{i=1}^{n}\left[y_{\mathrm{exp}}(i) - y_{\mathrm{num}}(i)\right]^2}{n}}\frac{100\%}{\mathscr{N}}, \qquad (11)$$

where y_{exp} denotes the experimental quantity, y_{num} is the corresponding numerical quantity, and n defines the signal length via the number of samples. The root–mean–square error is normalised by the normalisation factor, $\mathscr{N}$, which corresponds to the experimental peak value of the compared quantity.

4.1 Waves-only

Starting with the wave–only cases, Figures 10 (a)–(c) show the time traces of the target (experimental) and resulting (numerical) surface elevation for waves #1 – #3, respectively. While the peak amplitude is captured reasonably well in the numerical model, some differences in amplitude and phase[2] can be observed for the preceding and succeeding peaks and troughs. Comparing the three different waves, qualitatively largest deviations between the numerical and experimental data can be observed for wave #1.

For the quantitative comparison, based on the nRMSE (see Equation (11)), results are listed in Table 5. Overall, nRMSE values of $< 6\%$ are found for all three waves, with the largest value (5.5%) for wave #1, which is suggested by the qualitative analysis.

It should be noted here that no sensitivity study on the wave–generation settings (peak–wave amplitude, number of frequency components, etc.) has been conducted. Such a sensitivity analysis could, potentially, lead to an improvement of the agreement between the experimental and numerical data. However, as stated in Section 3.2.1, avoiding more laborious wave generation methods (e.g. [23]) significantly simplifies the model setup.

TABLE 5: nRMSE between the experimental target wave and the numerical surface elevation at the focal point for waves #1 – #3.

	Wave #1	Wave #2	Wave #3
nRMSE	5.5%	5.1%	4.3%

4.2 Wave-structure interaction

After analysing the wave–only cases, WSI cases are considered for which the floating structure is located at the focal point of the wave group in the NWT. For the comparison to the experimental reference data, mooring forces, as well as surge, heave, and pitch displacements are analyzed. Figures 11–13 show the time traces for wave #1 – #3, respectively.

Qualitatively analysing[3] the surge displacement of the float-

[2]It should be noted here that the time traces have been aligned in time based on the location of the peak amplitude in a post–processing step.

[3]Note that a quantitative analysis if omitted for the WSI cases, since the deviations are well visible through qualitative inspection.

Copyright © 2021 by ASME

Downloaded from http://asmedigitalcollection.asme.org/OMAE/proceedings-pdf/OMAE2021/85192/V009T09A027/6780842/v009t09a027-omae2021-62774.pdf by NTNU Universitets Biblioteket user on 01 April 2022

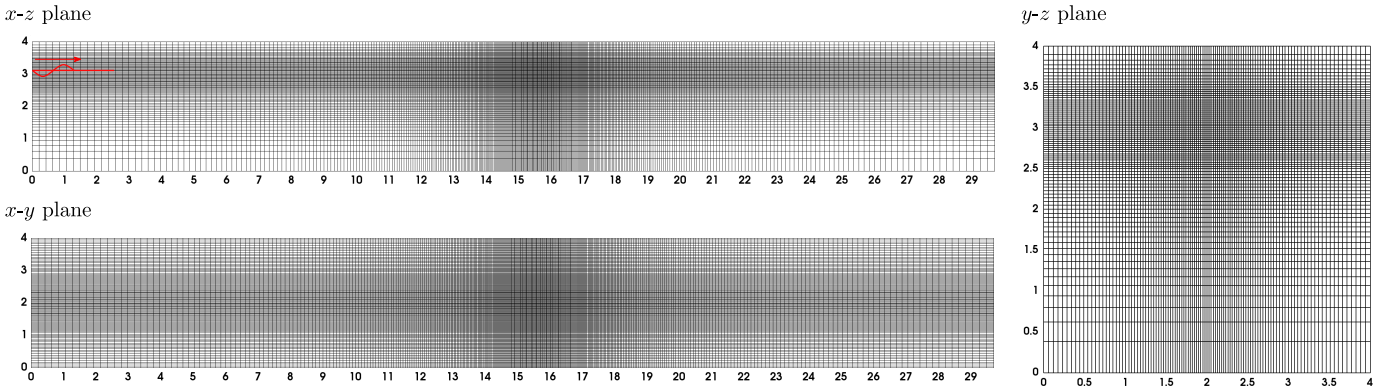

FIGURE 9: Plane views of the grid layout. All dimensions are in [m]. Waves are travelling in the x-direction.

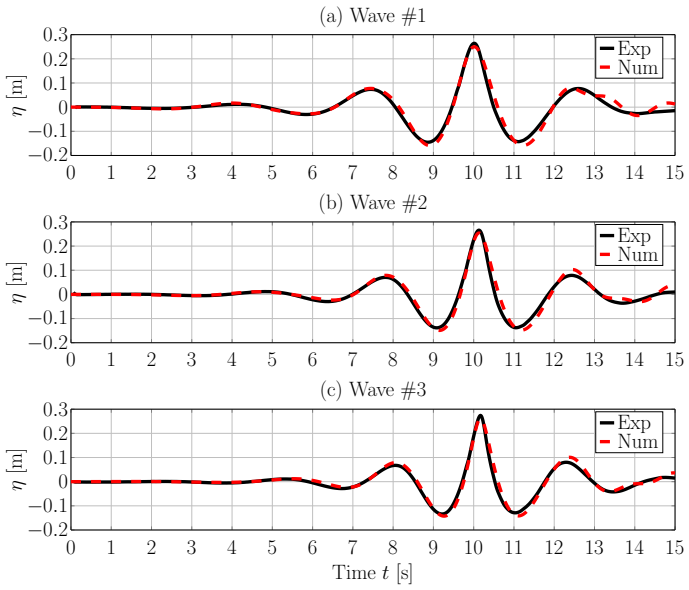

FIGURE 10: Target and resulting surface elevation for waves #1 (a), #2 (b), and #3 (c).

ing structure (Figures 11–13 (a)), a similar trend can be observed for all three waves. Up to the main peak surge displacement ($t \approx 10\,\text{s}$), acceptable agreement between the numerical and experimental data in phase and amplitude is achieved, showing some characteristic over-prediction of the second peak ($t \approx 8\,\text{s}$). Past the main peak, more significant differences in amplitude and phase between the experimental and numerical data set are visible. For wave #2 and #3 the surge displacement is over predicted in the numerical model, while for wave #1 an under prediction within the numerical model can be observed.

Similar trends for the different waves can also be observed for the heave displacement. A constant, small, phase shift ($\approx 0.15\text{s}$) can be observed. Furthermore, notable differences can be observed towards the end of the time traces for $t > 10\text{s}$. Based on the findings in [23], it can be assumed that the differences in the heave displacement are closely connected to the differences in the free surface elevation signal. A further correlation is identified in [23] between the heave displacement and mooring forces. From Figures 11–13 (b)/(d), this can be confirmed with the present results.

Finally, the pitch displacement is analysed. For wave #2 and #3, as for the surge/heave displacement and the mooring force, similar trends can be observed. The amplitude of the pitch displacement is captured relatively well, while notable differences in the phase of the oscillations are visible, in particular towards the end of the signal. For wave #1, relatively large deviations in phase and amplitude can be observed in Figures 11 (c). In particular after the main peak in the signal ($11\,\text{s} < t < 13\,\text{s}$), the numerically measured oscillation amplitudes are significantly under-predicted, compared with the experimental counterpart. Further investigation, in particular on the grid resolution, is required to determine the source of the large deviations for the pitch displacement.

5 Conclusions

This paper shows the validation of a NWT, based on the open–source CFD modelling toolbox REEF3D, against experimental reference data for a taut–moored, floating structure. The study forms the stepping stone towards the modelling of TLP-type floating offshore wind systems.

Results from wave–only test cases highlight the simplicity and effectiveness of the wave generation method, implemented in REEF3D. Without laborious calibration procedures or excessive pre–processing of the target wave data, relatively good agreements between the target (experimental) and resulting (numerical) free surface elevation time traces is achieved, with overall nRMSEs of $< 6\%$. For the WSI test cases, larger deviations between the experimental and numerical data can be observed, in particular for the surge and pitch displacements.

Copyright © 2021 by ASME

Downloaded from http://asmedigitalcollection.asme.org/OMAE/proceedings-pdf/OMAE2021/85192/V009T09A027/6780842/v009t09a027-omae2021-62774.pdf by NTNU Universitets Biblioteket user on 01 April 2022

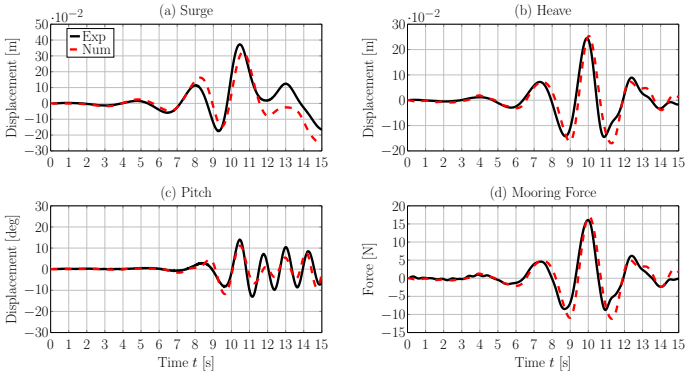

FIGURE 11: Numerical and experimental surge (a), heave (b), and pitch (c) displacement, as well as mooring force (d) for wave #1.

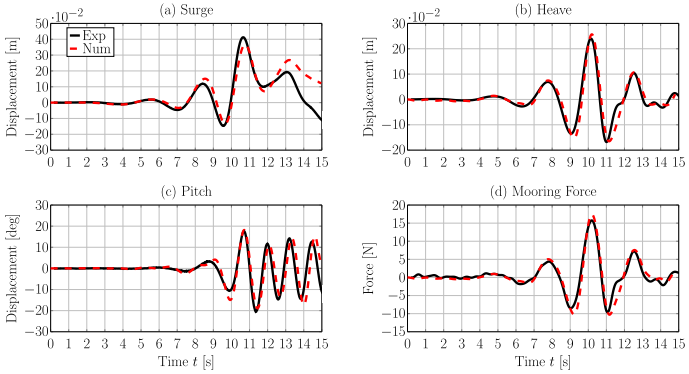

FIGURE 12: Numerical and experimental surge (a), heave (b), and pitch (c) displacement, as well as mooring force (d) for wave #2.

A more detailed investigation towards the influence of the grid resolution on the WSI simulations, in particular with regard to capturing boundary layer effects, is part of pertinent future work. To that end, simulations of the second of the two structures of the CCP-WSI Blind Test Series 2/3 (i.e. cylinder with sharp corners and a moon-pool) shall be considered. Furthermore, future work must embrace the modelling of irregular sea states and the response of a more realistic floating offshore wind systems. Overall, it can be concluded that the open–source CFD toolbox REEF3D shows potential to be used for the modelling of taut–moored structures for floating offshore wind applications.

ACKNOWLEDGMENT

This paper is based upon work supported by the German Federal Ministry for Economic Affairs and Energy under Grant No. 03SX524A. Hans Bihs and Tobias Martin are supported by the Research Council of Norway under the HAVBRUK2 project (No. 267981). Furthermore, the authors would like to acknowledge the CCP-WSI, funded by the Engineering and Physical Sciences Research Council (EPSRC) through projects EP/M022382/1, EP/S000747/1, and EP/P026109/1, for providing the experimental reference data.

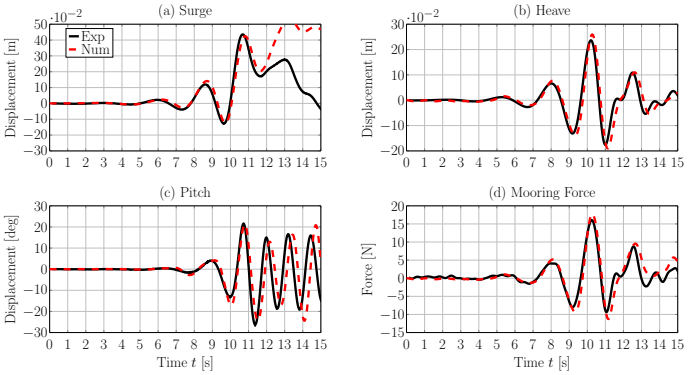

FIGURE 13: Numerical and experimental surge (a), heave (b), and pitch (c) displacement, as well as mooring force (d) for wave #3.

REFERENCES

[1] Hall, M., Buckham, B., and Crawford, C., 2014. "Evaluating the importance of mooring line model fidelity in floating offshore wind turbine simulations". Wind energy, **17**(12), pp. 1835–1853.

[2] Nematbakhsh, A., Bachynski, E. E., Gao, Z., and Moan, T., 2015. "Comparison of wave load effects on a TLP wind turbine by using computational fluid dynamics and potential flow theory approaches". Applied Ocean Research, **53**, pp. 142–154.

[3] Adam, F., Behr, C., Walia, D., Ritschel, U., Großmann, J., et al., 2017. "A modular TLP floating substructure to maximize the flexibility within the supply chain". In Proceedings of the 27th International Ocean and Polar Engineering Conference, San Francisco, CA, USA, International Society of Offshore and Polar Engineers, pp. 1–5.

[4] Ren, N., Li, Y., and Ou, J., 2014. "Coupled wind-wave time domain analysis of floating offshore wind turbine based on Computational Fluid Dynamics method". Journal of Renewable and Sustainable Energy, **6**(2), p. 023106.

[5] Quallen, S., Xing, T., Carrica, P., Li, Y., Xu, J., et al., 2014. "CFD simulation of a floating offshore wind turbine system using a quasi-static crowfoot mooring-line model". Journal of Ocean and Wind Energy, **1**(3), pp. 143—152.

[6] Quallen, S., and Xing, T., 2016. "CFD simulation of a floating offshore wind turbine system using a variable-speed generator-torque controller". Renewable Energy, **97**, pp. 230–242.

[7] Liu, Y., Xiao, Q., Incecik, A., Peyrard, C., and Wan, D., 2017. "Establishing a fully coupled CFD analysis tool for

Downloaded from http://asmedigitalcollection.asme.org/OMAE/proceedings-pdf/OMAE2021/85192/V009T09A027/6780842/v009t09a027-omae2021-62774.pdf by NTNU Universitets Biblioteket user on 01 April 2022

Copyright © 2021 by ASME

floating offshore wind turbines". Renewable Energy, **112**, pp. 280–301.

[8] Tran, T. T., and Kim, D.-H., 2018. "A CFD study of coupled aerodynamic-hydrodynamic loads on a semisubmersible floating offshore wind turbine". Wind Energy, **21**(1), pp. 70–85.

[9] Burmester, S., Vaz, G., and el Moctar, O., 2020. "Towards credible CFD simulations for floating offshore wind turbines". Ocean Engineering, **209**, p. 107237.

[10] Burmester, S., Vaz, G., Gueydon, S., and el Moctar, O., 2020. "Investigation of a semi-submersible floating wind turbine in surge decay using CFD". Ship Technology Research, **67**(1), pp. 2–14.

[11] Bihs, H., Kamath, A., Chella, M. A., Aggarwal, A., and Arntsen, Ø. A., 2016. "A new level set numerical wave tank with improved density interpolation for complex wave hydrodynamics". Computers & Fluids, **140**, pp. 191–208.

[12] Ransley, E., Brown, S., Hann, M., Greaves, D., Windt, C., Ringwood, J., Davidson, J., Schmitt, P., Yan, S., Wang, J. X., Wang, J. H., Ma, Q., Xie, Z., Giorgi, G., Hughes, J., Williams, A., Masters, I., Lin, Z., Chen, H., Qian, L., Ma, Z., Chen, Q., Ding, H., Zang, J., van Rij, J., Yu, Y., Li, Z., Bouscasse, B., Ducrozet, G., and Bingham, H., 2020. "Focused wave interactions with floating structures: A blind comparative study". Proceedings of the Institution of Civil Engineers - Engineering and Computational Mechanics, **0**(0), pp. 1–16.

[13] Ransley, E., Yan, S., Brown, S., Hann, M., Graham, D., Windt, C., Schmitt, P., Davidson, J., Ringwood, J., Musiedlak, P.-H., Wang, J., Wang, J., Ma, Q., Xie, Z., Zhang, N., Zheng, X., Giorgi, G., Chen, H., Lin, Z., Qian, L., Ma, Z., Bai, W., Chen, Q., Zang, J., Ding, H., Cheng, L., Zheng, J., Gu, H., Gong, X., Liu, Z., Zhuang, Y., Wan, D., Bingham, H., and Greaves, D., 2020. "A blind comparative study of focused wave interactions with floating structures (CCP-WSI Blind Test Series 3)". International Journal of Offshore and Polar Engineering, **30**(1), pp. 1–10.

[14] Ferziger, J. H., Perić, M., and Street, R. L., 2002. Computational methods for fluid dynamics, Vol. 3. Springer.

[15] Windt, C., Davidson, J., Schmitt, P., and Ringwood, J. V., 2019. "Contribution to the CCP-WSI Blind Test Series 2: CFD-based numerical wave tank experiments employing an impulse source wave maker". Proceedings of the 13th European wave and tidal energy conference (EWTEC), Naples, Italy.

[16] Jiang, G., and Shu, C., 1996. "Efficient implementation of weighted ENO schemes". Journal of Computational Physics, **126(1)**, pp. 202–228.

[17] Jiang, G., and Peng, D., 2000. "Weighted ENO schemes for Hamilton Jacobi equations". SIAM Journal of Scientific Computing, **21**, pp. 2126–2143.

[18] Timmermans, L., Minev, P., and Van De Vosse, F., 1996. "An approximate projection scheme for incompressible flow using spectral elements". International Journal for Numerical Methods in Fluid, **22**, pp. 673–688.

[19] Shu, C., and Osher, S., 1988. "Efficient implementation of essentially non-oscillatory shock-capturing schemes". Journal of Computational Physics, **77(2)**, pp. 439–471.

[20] van der Vorst, H., 1992. "BiCGStab: A fast and smoothly converging variant of Bi-CG for the solution of nonsymmetric linear systems". SIAM Journal of Scientific Computing, **Volume 13**, pp. 631–644.

[21] Osher, S., and Sethian, J., 1988. "Fronts propagating with curvature-dependent speed: Algorithms based on Hamilton-Jacobi formulations". Journal of Computational Physics, **79**, pp. 12–49.

[22] Sussman, M., Smereka, P., and Osher, S., 1994. "A level set approach for computing solutions to incompressible two-phase flow". Journal of Computational Physics, **114**, pp. 146–159.

[23] Windt, C., Davidson, J., Schmitt, P., and Ringwood, J. V., 2020. "Wave–structure interaction of wave energy converters: a sensitivity analysis". Proceedings of the Institution of Civil Engineers - Engineering and Computational Mechanics, **173**(3), pp. 144–158.

[24] Brown, S. A., Ransley, E. J., Musiedlak, P.-H., Greaves, D., et al., 2020. "Quantifying the predictive capability of OpenFOAM 5.0: Focused wave impacts with floating bodies". International Journal of Offshore and Polar Engineering, **30**(01), pp. 20–27.

[25] Yang, L., 2018. "One-fluid formulation for fluid–structure interaction with free surface". Comput. Methods Appl. Mech. Engrg., **332**, pp. 102–135.

[26] Martin, T., Tsarau, A., and Bihs, H., 2020. "A numerical framework for modelling the dynamics of open ocean aquaculture structures in viscous fluids". Applied Ocean Research, **In Press**. doi: 10.1016/j.apor.2020.102410.

[27] Martin, T., Kamath, A., and Bihs, H., 2020. "Accurate modeling of the interaction of constrained floating structures and complex free surfaces using a new quasistatic mooring model". International Journal for Numerical Methods in Fluids.

[28] Cummins, C., Viola, I. M., Mastropaolo, E., and Nakayama, N., 2017. "The effect of permeability on the flow past permeable disks at low Reynolds numbers". Physics of Fluids, **29**(9), p. 097103.

Downloaded from http://asmedigitalcollection.asme.org/OMAE/proceedings-pdf/OMAE2021/85192/V009T09A027/6780842/v009t09a027-omae2021-62774.pdf by NTNU Universitets Biblioteket user on 01 April 2022

Copyright © 2021 by ASME